

Motion Planning and Control of an Overactuated 4-Wheel Drive with Constrained Independent Steering

Shiyu Liu, Ilija Hadžić, Akshay Gupta, and Aliasghar Arab

Abstract— This paper addresses motion planning and control of an overactuated 4-wheel drive train with independent steering (4WIS) where mechanical constraints prevent the wheels from executing full 360-degree rotations (swerve). The configuration space of such a robot is constrained and contains discontinuities that affect the smoothness of the robot motion. We introduce a mathematical formulation of the steering constraints and derive discontinuity planes that partition the velocity space into regions of smooth and efficient motion. We further design the motion planner for path tracking and obstacle avoidance that explicitly accounts for swerve constraints and the velocity transition smoothness. The motion controller uses local feedback to generate actuation from the desired velocity, while properly handling the discontinuity crossing by temporarily stopping the motion and repositioning the wheels. We implement the proposed motion planner as an extension to ROS Navigation package and evaluate the system in simulation and on a physical robot.

I. INTRODUCTION

Four-wheel drive with independent steering (4WIS) is a mobility mechanism in which each wheel is actuated by two dedicated motors — one for steering and one for driving — enabling independent steering and drive. This drivetrain can theoretically achieve three degrees of freedom (3-DOF) with zero side-slip forces [1], which enables low tire wear, energy efficiency, and smooth, versatile maneuvers. Kinematic and dynamic control methods for this drivetrain have been extensively studied [2]–[6]. All reported work assumes unconstrained steering, that is, the ability for the wheel to perform a full 360-degree swerve.

Although simple mechanical construction of a full-swerve wheel exists [7], very often chassis design or cabling constraints limit the rotation range of the steering shaft [8]–[10]. These systems typically sidestep the issue by operating in three discrete modes: longitudinal or lateral Ackermann steering, along with an option for in-place rotation.

In this paper, we propose a cascade controller that unifies constrained and unconstrained case. Steering constraints are expressed through so-called *discontinuity planes*, which dissolve for unconstrained case. We integrate the controller with the Robot Operating System (ROS) Navigation package [11], which is a commonly used software platform for many research and industrial robots. Although it is possible to formulate the steering constraints in a dynamic model, and design the controller based on more sophisticated algorithms

such as MPC [12], [13], we opt for a cascaded architecture to fit the architecture of ROS Navigation stack. In this architecture, the global planner generates the trajectory as a set of waypoints, the local planner selects the optimal velocity taking into account kinematic and dynamic constraints, and the motion controller produces the actuation that satisfies steering constraints. The baseline local planner in ROS Navigation package is derived from Dynamic Window Approach (DWA) [14] planner, which we also use as the baseline for our system.

II. SYSTEM ARCHITECTURE

Figure 1(a) shows an in-house-built 4WIS drive that we use to develop the controller and conduct the experiments. The hardware consists of four hub-wheels with embedded drive-motors, each mounted on a rotary mechanism driven by a dedicated steering motor. The drive-motor power supply lines and encoder wires extend from the motor controller, mounted on the chassis, to the motor and they twist as the wheel steers. Conduits and fenders prevent the wires from rubbing the spinning wheel, but the whole cable-management mechanism also prevents the steering mechanism from performing a full 360-degree swerve. It is this limitation that imposes kinematic constraints that the controller must observe during the motion and during transitions from one velocity to another. Such constrained-swerve steering mechanism has been practically witnessed in many industrial 4WIS platforms [8]–[10].

Figure 1(b) shows the annotated top-view diagram used for modeling. Geometric parameters w_l , w_r , l_f , and l_r define the position of the wheels in the local frame of reference $\mathcal{F}_G(\mathbf{x}, \mathbf{y})$. Body velocity is denoted as $\mathbf{v} = [v_x \ v_y \ \dot{\psi}]^T$ where v_x , v_y are linear velocity components in $\mathcal{F}_G(\mathbf{x}, \mathbf{y})$, and $\dot{\psi}$ is the angular velocity (yaw rate). The wheel radius is denoted as r_w . The wheels' angular velocities around the rotating shaft are given by $\boldsymbol{\omega} = [\omega_1 \ \omega_2 \ \omega_3 \ \omega_4]^T$, and their linear velocities are defined by $\mathbf{v}_w = [v_1 \ v_2 \ v_3 \ v_4]^T$. The steering angles of the wheels are denoted by $\boldsymbol{\delta} = [\delta_1 \ \delta_2 \ \delta_3 \ \delta_4]^T$. The order of all vector components with index $i \in \{1, 2, 3, 4\}$ follows the convention: front-left, rear-left, rear-right and front-right.

The objective of motion control is to deliver the sequence of velocity vectors \mathbf{v} in $\mathcal{F}_G(\mathbf{x}, \mathbf{y})$ that advances the robot towards the goal or the next waypoint \mathbf{q}_d in the reference frame $\mathcal{F}_O(\mathbf{X}, \mathbf{Y})$. The motion is smooth if the generated sequence successfully avoids constraints. When such avoidance is not possible, the robot must temporarily stop the motion and reposition the wheels before continuing. The constraints

The work reported in the paper was performed in its entirety while Liu was affiliated with Nokia Bell Labs, France and Arab was affiliated with Nokia Bell Labs, USA. Hadžić and Gupta are with Nokia Bell Labs, USA and Arab is now with New York University, Tandon School of Engineering, Mechanical and Aerospace Engineering Department.

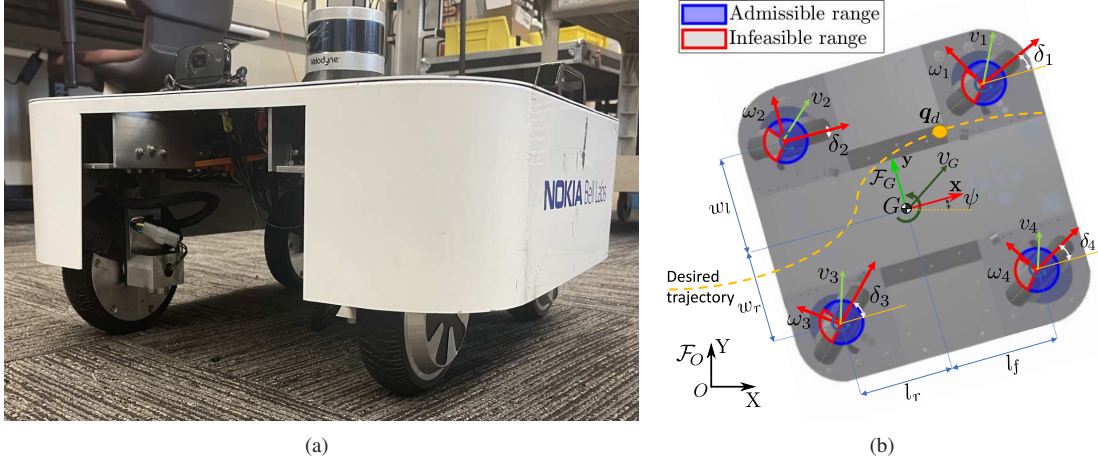


Fig. 1. A 4-wheel drive with independent steering (4WIS) robot: (a) front view of the experimental model and (b) top view diagram of the drivetrain.

are kinematic in nature, but they exist regardless of whether the controller is kinematic or dynamic.

III. STEERING WHEEL CONSTRAINTS

We first derive the steering constraints presented above. From 4WIS inverse kinematics [13], it is straightforward to show that for a given velocity vector, the wheel positions are

$$\delta = \begin{bmatrix} \text{atan2} \left(v_y + l_f \dot{\psi}, v_x - w_l \dot{\psi} \right) \\ \text{atan2} \left(v_y - l_r \dot{\psi}, v_x - w_l \dot{\psi} \right) \\ \text{atan2} \left(v_y - l_r \dot{\psi}, v_x + w_r \dot{\psi} \right) \\ \text{atan2} \left(v_y + l_f \dot{\psi}, v_x + w_r \dot{\psi} \right) \end{bmatrix}. \quad (1)$$

From Fig. 1(b), steering-wheel constraints are expressed as

$$\delta_i \in \Omega_\delta = [\delta_{\min}, \delta_{\max}], \quad \text{for } i \in \{1, 2, 3, 4\}, \quad (2)$$

resulting in eight inequalities (two per wheel) that determine a set of admissible velocity configurations \mathcal{V} represented by

$$\mathbf{v} \in \mathcal{V} = \bigcap_{i \in \{1, 2, 3, 4\}} \mathcal{V}_i \subseteq \mathbb{R}^3 \quad (3)$$

where \mathcal{V}_i is defined as a subset of velocity configurations that the robot's velocity vector \mathbf{v} can reach without violating the steering angle limits imposed by the i th wheel:

$$\mathcal{V}_i = \left\{ \mathbf{v} \mid (\mathbf{b}_i^{(1)})^T \mathbf{v} > 0, (\mathbf{b}_i^{(2)})^T \mathbf{v} > 0 \right\}. \quad (4)$$

$\mathbf{b}_i^{(1)}, \mathbf{b}_i^{(2)}$ are vectors factorizing the velocity vector \mathbf{v} to formulate inequality constraints associated with the steering angle limits (i.e., $\delta_i < \delta_{\max}$ and $\delta_i > \delta_{\min}$). We derive inequality conditions starting from (3) and (4), considering any given velocity configuration. First, we establish certain properties of the steering limits.

If the steering angle limits satisfy $\delta_{\min} \leq -\pi$ and $\delta_{\max} \geq \pi$ conditions, then a solution that satisfies (3) exists for each steering wheel δ_i in (1) and for any given velocity configuration $\mathbf{v} \in \mathbb{R}^3$. Recall the property of atan2 function,

whose range is $(-\pi, \pi]$. So any δ_i computed from (1) is a valid solution without crossing the steering angle limits.

If $\delta_{\min} \in (-\pi, -\frac{\pi}{2}]$ and $\delta_{\max} \in [\frac{\pi}{2}, \pi)$, there exists *at least* one solution for any given velocity configuration $\mathbf{v} \in \mathbb{R}^3$, but some solutions may violate the steering limits, in which case, the robot can achieve the same velocity by switching the rotation direction of the drive wheels and flipping the steering angles δ_i :

$$\delta_i, \omega_i = \begin{cases} \delta_i, \omega_i & \delta_i \in \Omega_\delta \\ \delta_i - \pi \text{sign}(\delta_i), -\omega_i & \delta_i \notin \Omega_\delta \end{cases}. \quad (5)$$

The $\text{sign}(\cdot)$ is the sign function and ω_i is the rotational velocity of the i th drive motor.

A. Discontinuity Planes

The inequality constraints defined in (4), imposed by the steering angle limits, form *discontinuity planes* in the robot's velocity configuration space. These discontinuity planes are solved by imposing the equality constraints for each wheel as $(\mathbf{b}_i^{(1)})^T \mathbf{v} = 0$ and $(\mathbf{b}_i^{(2)})^T \mathbf{v} = 0$, for $i \in \{1, 2, 3, 4\}$. The motion remains smooth if the trajectory through the velocity space formed by changing velocity does not cross any discontinuity plane. Figure 2 shows the discontinuity planes for conditions discussed herein.

1) $\delta_{\max} = -\delta_{\min} = \frac{\pi}{2}$: Figure 2(a) shows the configuration space split in four continuous regions by two discontinuity planes. This is a special case in which eight constraints collapse into only two planes. Specifically, when the output of atan2 function in (1) is $\pm \frac{\pi}{2}$ the discontinuity planes for four wheels reduce to

$$\begin{aligned} v_x - w_l \dot{\psi} &= 0 \quad (\text{for wheels 1 and 2}) \\ v_x + w_r \dot{\psi} &= 0 \quad (\text{for wheels 3 and 4}), \end{aligned} \quad (6)$$

that is $x = 0$ for $\text{atan2}(y, x) = \pm \frac{\pi}{2}$.

To avoid stopping the robot to reverse the rotational direction of the wheels, it is preferred to keep the configuration within one of the two larger regions of Fig. 2(a). If we further

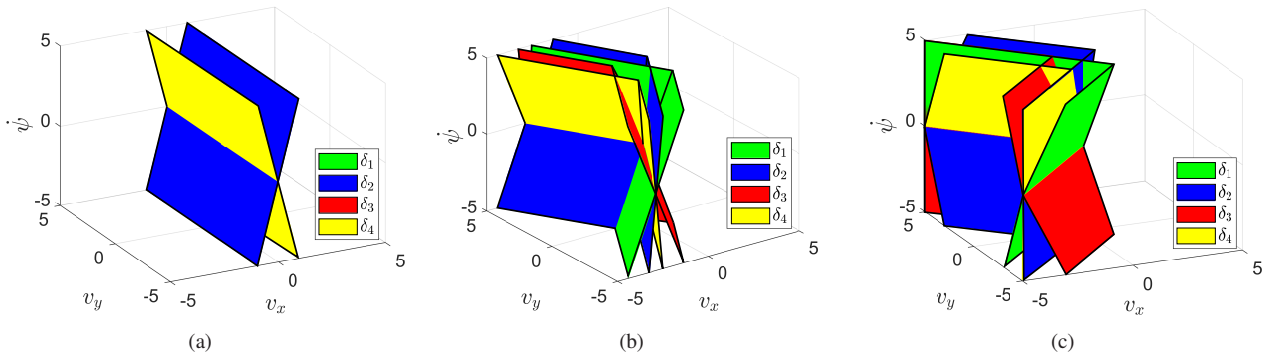


Fig. 2. Discontinuity planes in the 3D velocity configuration space. (a) $\Omega_\delta = [-\frac{\pi}{2}, \frac{\pi}{2}]$; (b) $\Omega_\delta = [-\frac{2\pi}{3}, \frac{2\pi}{3}]$; (c) $\Omega_\delta = [-\frac{3\pi}{4}, \frac{3\pi}{4}]$.

assume that forward-motion is preferred, the constraints are

$$\begin{aligned} v_x - w_l \dot{\psi} &> 0 \\ v_x + w_r \dot{\psi} &> 0. \end{aligned} \quad (7)$$

2) $\delta_{\max} = -\delta_{\min} \in (\frac{\pi}{2}, \pi)$: Figure 2(b) and 2(c) show two instances of a general case where the configuration space is split in 12 continuous regions by 8 discontinuity planes (i.e., two constraints per wheel). Considering (1) and the steering limits in (2), the discontinuity planes corresponding to two steering constraints for the i -th wheel can be given by

$$\begin{aligned} \tan(\delta_{\max})(v_x + w_i \dot{\psi}) - (v_y + l_i \dot{\psi}) &= 0 \\ \tan(\delta_{\min})(v_x + w_i \dot{\psi}) - (v_y + l_i \dot{\psi}) &= 0, \end{aligned} \quad (8)$$

with additional constraints $v_x + w_i \dot{\psi} < 0$, where $w_i \in \{-w_l, -w_l, w_r, w_r\}$ and $l_i \in \{l_f, -l_r, -l_r, l_f\}$, for $i \in \{1, 2, 3, 4\}$. By factorizing (8) with respect to v , $\mathbf{b}_i^{(1)}$ and $\mathbf{b}_i^{(2)}$ can be derived as

$$\begin{aligned} \mathbf{b}_i^{(1)} &= [\tan(\delta_{\max}) \quad -1 \quad (w_i \tan(\delta_{\max}) - l_i)] \\ \mathbf{b}_i^{(2)} &= [\tan(\delta_{\min}) \quad -1 \quad (w_i \tan(\delta_{\min}) - l_i)]. \end{aligned} \quad (9)$$

By grouping $\mathbf{b}_i^{(1)}$ and $\mathbf{b}_i^{(2)}$ for all four wheels, the 8 discontinuity planes are the solutions of $\mathbf{B}\mathbf{v} = \mathbf{0}$, where $\mathbf{B} \in \mathbb{R}^{8 \times 3}$ is defined as

$$\mathbf{B} = \begin{bmatrix} -\tan(\delta_{\max}) & 1 & (l_f + w_l \tan(\delta_{\max})) \\ -\tan(\delta_{\max}) & 1 & -(l_r - w_l \tan(\delta_{\max})) \\ -\tan(\delta_{\max}) & 1 & -(l_r + w_r \tan(\delta_{\max})) \\ -\tan(\delta_{\max}) & 1 & (l_f - w_r \tan(\delta_{\max})) \\ \tan(\delta_{\min}) & -1 & -(l_f + w_l \tan(\delta_{\min})) \\ \tan(\delta_{\min}) & -1 & (l_r - w_l \tan(\delta_{\min})) \\ \tan(\delta_{\min}) & -1 & (l_r + w_r \tan(\delta_{\min})) \\ \tan(\delta_{\min}) & -1 & -(l_f - w_r \tan(\delta_{\min})) \end{bmatrix}, \quad (10)$$

with constraints $v_x - w_l \dot{\psi} < 0$ for wheels 1 and 2, and $v_x + w_r \dot{\psi} < 0$ for wheels 3 and 4. In (10) rows i and $i + 4$ come from wheel i , vectors that are represented by $\mathbf{b}_i^{(1)}$, $\mathbf{b}_i^{(2)}$ in (9) and correspond to the conditions $\delta_i = \delta_{\max}$ and $\delta_i = \delta_{\min}$ respectively, where $i \in \{1, 2, 3, 4\}$. Note that the additional conditions $v_x - w_l \dot{\psi} < 0$ and $v_x + w_r \dot{\psi} < 0$ prevent the configuration space to be over-constrained, that is $x < 0$ for $\text{atan2}(y, x) \in (\frac{\pi}{2}, \pi)$. It is also worth noting that

the first four rows of (10) are equivalent to the expressions in the first row of (9); the negative signs are used solely to distinguish between the conditions $\delta_i = \delta_{\max}$ and $\delta_i = \delta_{\min}$.

There is only one large region, which is the most desirable one to keep the configuration vector in. Note that the existence of many small regions associated with $v_x < 0$ will cause the wheels to flip often if the robot is moving in reverse direction. To keep the number of wheel flips low, backward motion should be kept within the second largest region (behind all discontinuity planes). We specify these two regions as the preferred regions and make it the motion planner's responsibility to generate the velocities within them.

B. Region Signature

A generic way to determine the region for a given velocity vector \mathbf{v} is to calculate

$$\mathbf{s} = \frac{1}{2} \left(\text{sign}(\mathbf{B}\mathbf{v}) + \mathbf{1}_{8 \times 1} \right), \quad (11)$$

where $\text{sign}(\cdot)$ is the sign function applied to a vector component-wise.

The resulting vector \mathbf{s} , which we call the *region signature*, indicates the region in which the velocity vector resides. Specifically, $s_j = 1$ indicates that \mathbf{v} is ahead of the plane j defined by the constraint of the j th row of \mathbf{B} . Vector \mathbf{s} can be interpreted as binary-encoded unsigned integer and used as an index into a lookup table that retrieves the ID of one of the 12 regions partitioned by the 8 discontinuity planes. The numerical values of the region IDs are visualized in Fig. 3. The solution space for (11) does not span the full 8-bit integer space. Instead, there are only 46 possible solutions, which in turn map to 12 different regions (multiple solutions correspond to the same region).

Region 0 is the largest continuous region shown in Fig. 2(b) and Fig. 2(c) and is typically the preferred region of the configuration space. It corresponds to the robot moving primarily forward and sideways. Region 1 is the second largest region and corresponds to the generally backwards motion. Other regions are not preferred because they are small and thus likely to trigger the transition through discontinuity planes, which requires the robot to stop and reposition the wheels.

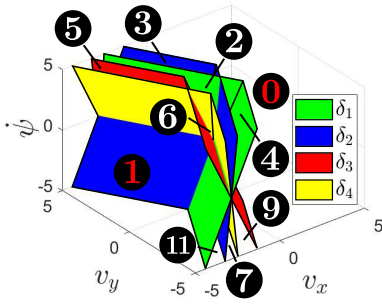


Fig. 3. Definition of 12 continuous regions in the velocity configuration space. Note that regions with ID 8 and 10 are hidden at the bottom of the left halves of the planes. Regions with IDs 0 and 1 (red) are preferred.

The design objective of the motion planner is to generate a time-series of velocities that advances the robot towards the goal, steer clear of obstacles and avoid crossing the discontinuity planes whenever possible. The last requirement is not a hard constraint but rather a strong preference. The planner should do the best effort to keep the generated velocity in region 0 (preferred region) or region 1 (second-preferred region), and cross into other (non-preferred) regions only when forced by other constraints. Once in a non-preferred region, the planner can trade off between restricting itself to the new and smaller region or taking the penalty to transition back to the preferred region where it has more options for selecting the velocity vectors. In either case, the region signature of the present and the previous velocity can be used as an input to a cost function that controls the selection of the velocity vector.

IV. PLANNER IMPLEMENTATION

The principles presented thus far are valid for any navigation stack that follows the cascade architecture. The constraints that we derived belong to the local planner, which generates velocity commands based on the waypoint the robot is trying to reach and the cost map constructed from observed obstacles. The motion controller, which converts the velocity vector to actuation defends from discontinuity-plane crossing by stopping the motion if the wheel flip becomes necessary.

To evaluate our system in simulation and on a physical robot, we chose to implement the planner as an extension to the DWA [14] planner, which comes with the standard ROS Navigation [11] stack and gives us a well understood baseline to compare the results against.

A. DWA Planner

The “stock” DWA planner explores the space of velocities that are reachable from present velocity given robot dynamics. For each candidate velocity, $(v_x, v_y, \text{ and } \dot{\psi})$, DWA forward-simulates the near-term robot position and passes the projected paths to the chain of critic functions. Each critic computes the cost (or flags the velocity inadmissible) independently. The selected velocity is the admissible velocity with the lowest weighted sum produced by each critic.

Our implementation adds two new critics to the chain called *swerve-constraint critic*, and *smoothness critic*.

B. Swerve-Constraint Critic

The swerve-constraint critic penalizes velocities in non-preferred regions and velocities that cross from one region to the other. This requires access to both proposed velocity and present velocity. The former is generated by the planner, whereas the latter can either come from odometry feedback or the velocity command of the previous planning cycle.

We implement two scoring modes. In *simple scoring* mode, the critic first checks if the proposed velocity is in the same region as the present one. If so, it assigns zero-cost if the region is preferred, and half of the maximum cost, otherwise. Transitions into a non-preferred region are deemed inadmissible and all other transitions are penalized with the maximum cost. In *distance-based scoring* mode, transitions within the same region are penalized using exponentially decaying function of the distance to the nearest discontinuity plane (denoted by d_{\min}), with the cost given by

$$c_{\text{swerve}} = \alpha_{\text{swerve}} e^{-\gamma d_{\min}} \quad (12)$$

where α_{swerve} is the maximum cost for penalizing the violation of swerve constraints and γ is the decaying rate. This scoring policy reduces the probability of region crossing by keeping the velocity vector away from the discontinuity plane. The distance for velocity located in non-preferred regions is simply the minimum normal distance to all the discontinuity planes:

$$d_{\min} = \min_{j=[1,8]} \{d_j\}, \text{ with } d_j = \frac{\mathbf{B}[j, :] \mathbf{v}}{\|\mathbf{B}[j, :]\|}, \quad (13)$$

where $j \in [1, 8]$ is the plane index, $\mathbf{B}[j, :]$ is the j th row of the matrix \mathbf{B} , and $\|\cdot\|$ is the 2-norm of a vector. For region 1, the distance is the minimum distance to four discontinuity planes that form the region, namely the left halves of the planes for δ_2 and δ_4 , and the right halves for δ_1 and δ_3 . Region 0 is non-convex and the distance defined by (13) does not exist, so we use a modified metric. We first evaluate the velocity vector against two auxiliary planes $v_x - w_1 \dot{\psi} = 0$ and $v_x + w_1 \dot{\psi} = 0$. If the velocity is located behind either of two auxiliary planes, the distance is still that of (13). If the velocity vector is located ahead of these two auxiliary planes, we first find the projection of the velocity vector onto the nearest auxiliary plane and compute the distance, followed by adding the distance from that projection to the nearest constraint-plane (see Fig. 4).

The exception to the above-described policy is when the robot is starting the motion from a stationary or close-to-stationary state. In that case, the critic allows the velocity vector to transition to any region, because there is no notion of discontinuity. In practice, this allows the robot to use non-preferred regions when they are really needed, but as the motion starts, the configuration will gravitate towards preferred regions. Once in full motion, preferred regions will be used barring external disturbances, actuator errors,

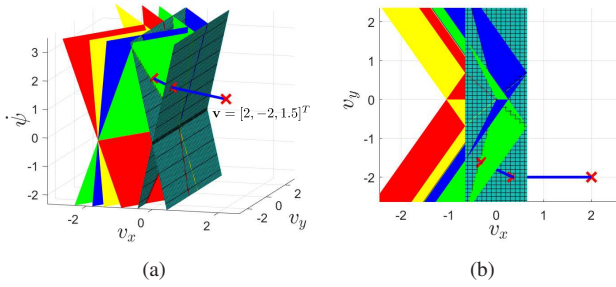


Fig. 4. Distance to the nearest discontinuity plane for a velocity vector located in region 0 and ahead of two auxiliary planes. (a) side view and (b) top view. Red markers show the original velocity vector, its projection onto the nearest auxiliary plane, followed by the projection onto the nearest discontinuity plane. The blue lines represent the resulting distance metric.

or tuning that makes other critics in the chain prevalent. If a non-preferred region is entered, the motion planner will try to transition the velocity configuration back into the preferred region as soon as such transition becomes possible.

Computational load per proposed velocity is relatively small. The critic must do 8 matrix multiplications of (13), where \mathbf{B} is static and can be pre-calculated at initialization time. The dimension of \mathbf{B} is 8×3 , which is considered small and the final cost (12) needs to be calculated only once for each proposed velocity.

C. Smoothness Critic

As the DWA planner executes the chain of critics, it may assign the same cost to multiple candidate velocities that are located far apart in the configuration space. Such scenarios commonly occur when navigating around obstacles or in narrow spaces where only a portion of the sampled velocities are admissible.

If a velocity previously commanded is deemed inadmissible in the next planning cycle, the planner might select another candidate velocity that may not necessarily trigger the discontinuity crossing, but still cause a large step change in wheel position. This can be harmful if wheels are controlled independently. Specifically, if one wheel gets ahead of the other the actuation may no longer correspond to any valid velocity configuration, which causes lateral friction.

A simple way to counter the problem is to make the planner prefer gradual transitions. The smoothness critic computes the distance to the previously commanded velocity and penalizes the proposed velocity linearly with the calculated distance. The cost of smoothness critic is computed as

$$c_{\text{smoothness}} = \alpha_{\text{smoothness}} \text{cap}(\mathbf{v}^d, \mathbf{v}^c) \quad (14)$$

with $\alpha_{\text{smoothness}}$ parametrizing the maximum cost of the smoothness critic, \mathbf{v}^d and \mathbf{v}^c being the proposed and the present velocity. The $\text{cap}(\cdot, \cdot)$ function is defined as

$$\text{cap}(\mathbf{v}^d, \mathbf{v}^c) = \begin{cases} \frac{\|\mathbf{v}^d - \mathbf{v}^c\|}{\Delta v_{\text{max}}}, & \text{if } \|\mathbf{v}^d - \mathbf{v}^c\| \leq \Delta v_{\text{max}}, \\ 1, & \text{otherwise,} \end{cases} \quad (15)$$

where $\|\cdot\|$ is the 2-norm of a vector and Δv_{max} determines the smallest velocity transition step penalized with the maximum cost.

Computational load per proposed velocity is trivial because the critic only needs to subtract the current and proposed velocity and compare the magnitude of the difference with a threshold.

V. EXPERIMENTAL RESULTS

We evaluate the performance both on physical hardware and in simulation using the Gazebo [15] package for high-fidelity physics modeling. The models capture full dynamics of the robot frame, motor dynamics, and contact points between wheels and the surface. Sensor noise and non-deterministic effects of wheel-surface interaction are also captured by the model and we do not reset the simulation world between runs. Consequently, stochastic effects seen in the physical world are also present in simulation.

Physical robot build has the wheel base $l_f = l_r = w_l = w_r = 0.2m$ and steering limits $\delta_{\text{max}} = -\delta_{\text{min}} = 130^\circ$. It is driven by brushless-motor hub-wheels of radius $0.08m$ and steered using a brushed DC motor. The motion-control/actuation loop runs at 100Hz, the local planner runs at 5Hz, and the global planner re-plans once per second.

The parameters for swerve-constraint and smoothness critics are set to the same values in both simulation and real-world experiments, which are $\alpha_{\text{swerve}} = 5.0$, $\alpha_{\text{smoothness}} = 2.0$, $\gamma = 20.0$, and $\Delta v_{\text{max}} = 0.2$. The maximum cost value for the swerve-constraint critic was selected such that its weight is about 60% of the weight of (standard DWA) path-distance and goal-distance critics. In this way, progress towards the goal and remaining on the planned path is the priority, but motions that are likely to cause discontinuity are discouraged. The smoothness critic must have the smallest weight relative to other critics so that it does not interfere with the ability to follow the path and avoid obstacles. Fine tuning of these weights is done experimentally. Parameters γ and Δv_{max} were preliminary determined through simulation to ensure efficiency, specifically by providing an appropriate decay rate and a representative velocity difference for characterizing non-smoothness.

A. Experiments

For each test case, we issue a sequence of goals that make the robot follow an established nominal path. For each run, we measure the time to complete the trajectory and count the wheel-flip events due to discontinuity-plane crossings. For both metrics, the lower value indicates better performance.

The paths we use include simple patterns, such as rectangle, figure-x and figure-8 path, as well as a more complex path in which the robot navigates through a maze. The maze path consists of segments which expose the robot to a variety of maneuvers, such as turns, change in direction, rotation, sideways motion, and backwards motion. The nominal path for each scenario is the same, but environment variations may produce slightly different waypoint coordinates for different runs, which in turn impacts the discontinuity results. For each

scenario, we repeat the test 10 times to ensure that the results are repeatable and to quantify the robot behavior variability.

We evaluate the planner in simple-scoring mode and distance-based scoring mode. For both modes, we evaluate the case when only region 0 is preferred (referred to as the forward-only critic) and the case where both region 0 and 1 are preferred (referred to as the forward-backward critic). All other regions are non-preferred.

We compare the performance of our augmented DWA planner with two baseline cases: 1) “stock” DWA planner with basic motion controller, and 2) “stock” DWA planner with motion controller that picks the wheel orientation that results in the shortest angle transition if the kinematic solution yields two valid orientations. The latter helps with the stock planner, but can interfere with the augmented planner because the controller-side optimization can transition the wheel into the region that is inconsistent with planner’s belief.

B. Results

The planner configurations are detailed in Table I, and Table II (simulation) and Table III (physical robot) summarize the number of encountered discontinuities and travel time. We highlight the “winner” configuration according to each metric, which is selected by prioritizing a lower median value, alongside a reasonably low mean and a lower standard deviation, to ensure both typical performance and consistency across repeated runs.

TABLE I
CONFIGURATIONS OF THE EVALUATED PLANNERS.

Config. ID	Shortest transition	Scoring mode	Preferred regions
baseline-1	no	-	-
baseline-2	yes	-	-
aug-DWA-1	no	distance-based	forward-only
aug-DWA-2	no	distance-based	forward-backward
aug-DWA-3	no	simple-scoring	forward-only
aug-DWA-4	no	simple-scoring	forward-backward

Physical robot experiments show the same general trends as in the simulation, so in that sense they are consistent. The difference in absolute numbers is expected, because in simulation there is no room clutter that interferes with the localization system, wheel-surface interaction is more predictable, and the robot can recover from discontinuity crossings more easily and quickly.

The baseline planner performance appears very poor compared to all other configurations. In some runs the robot remained stuck thrashing the wheels, because the planner kept issuing the discontinuity-crossing velocities. This situation happens when the robot needs to move in the direction of the diagonal formed by its center and one of its rear edge, putting the wheels at the boundary of the discontinuity plane. For this reason we had to abandon the physical-robot test for the baseline-1 configuration in the maze scenario. Although the shortest-transition enhancement in baseline-2 improved the stock DWA planner considerably, the advantage of using the

TABLE II
SIMULATION RESULTS: DISCONTINUITY COUNT AND TRAVEL TIME.

Scenario	Config. ID	Discontinuity count			Travel time (s)		
		mean	median	std	mean	median	std
figure-8	baseline-1	11.1	7.5	10.6	52.0	44.3	15.7
	baseline-2	3.7	3.0	2.7	39.7	39.5	2.3
	aug-DWA-1	1.2	1.0	1.2	38.4	37.1	2.6
	aug-DWA-2	1.2	1.0	0.6	38.5	38.3	1.3
	aug-DWA-3	1.6	1.5	0.7	37.3	37.3	1.4
	aug-DWA-4	1.5	1.0	1.0	38.4	38.4	1.6
figure-x	baseline-1	30.9	26.5	9.9	89.4	84.9	12.8
	baseline-2	5.9	6.5	3.4	62.3	61.6	5.4
	aug-DWA-1	4.2	4.0	2.0	59.3	58.2	5.8
	aug-DWA-2	2.2	2.0	1.9	56.0	56.0	6.5
	aug-DWA-3	5.8	6.0	1.6	64.4	67.2	7.3
	aug-DWA-4	3.1	4.0	2.2	59.1	58.3	8.7
rectangle	baseline-1	15.4	8.5	14.6	53.9	47.9	16.8
	baseline-2	5.5	6.0	2.2	42.7	43.7	3.4
	aug-DWA-1	1.5	1.0	1.0	39.5	39.5	1.9
	aug-DWA-2	2.2	2.5	1.2	39.4	38.9	1.7
	aug-DWA-3	3.3	3.5	2.7	41.9	40.8	4.2
	aug-DWA-4	2.6	2.5	1.4	39.0	38.6	1.8
maze	baseline-1	18.3	11.5	19.3	142.1	132.9	23.8
	baseline-2	7.3	8.0	3.7	128.1	128.2	3.2
	aug-DWA-1	3.3	3.0	1.0	123.3	122.8	2.1
	aug-DWA-2	2.3	2.5	1.2	124.1	123.1	3.7
	aug-DWA-3	4.2	4.0	1.9	125.6	125.8	2.9
	aug-DWA-4	2.6	2.5	1.7	123.1	122.7	2.1

TABLE III
PHYSICAL-ROBOT RESULTS: DISCONTINUITY COUNT AND TRAVEL TIME.

Scenario	Config. ID	Discontinuity count			Travel time (s)		
		mean	median	std	mean	median	std
figure-8	baseline-1	18.6	15.5	14.2	166.3	172.0	85.6
	baseline-2	4.8	5.0	3.3	76.9	76.7	24.4
	aug-DWA-1	1.4	1.0	2.2	46.4	40.3	13.5
	aug-DWA-2	2.0	2.0	1.8	50.1	48.8	10.2
	aug-DWA-3	2.2	1.5	2.5	52.8	47.3	18.3
	aug-DWA-4	1.5	1.0	1.6	48.4	49.3	12.6
figure-x	baseline-1	38.4	36.0	13.7	319.6	327.2	81.5
	baseline-2	8.4	9.0	3.2	153.9	164.2	52.2
	aug-DWA-1	6.8	7.0	1.6	87.3	88.3	6.7
	aug-DWA-2	4.3	4.0	2.5	72.4	70.2	10.1
	aug-DWA-3	8.4	6.5	4.2	97.2	100.9	21.8
	aug-DWA-4	5.6	5.5	2.4	90.8	88.1	15.2
rectangle	baseline-1	16.2	12.0	13.9	135.4	125.1	69.1
	baseline-2	2.2	2.0	0.92	53.9	53.6	9.0
	aug-DWA-1	1.7	1.5	1.2	48.1	48.1	7.7
	aug-DWA-2	1.8	2.0	1.3	50.5	51.3	6.9
	aug-DWA-3	1.7	1.0	1.4	47.6	44.5	8.9
	aug-DWA-4	2.0	2.0	1.1	53.7	52.5	9.1
maze	baseline-1*	35.3	16.0	41.5	337.0	204.2	265.1
	baseline-2	8.8	10	2.8	215.2	194.8	61.4
	aug-DWA-1	3.7	3.0	1.6	149.3	147.1	9.9
	aug-DWA-2	2.2	2.0	1.0	137.5	137.8	3.7
	aug-DWA-3	4.1	3.0	2.8	149.0	144.8	14.0
	aug-DWA-4	2.5	2.0	2.0	141.5	139.4	8.1

*Baseline-1 maze-test abandoned due to incessant wheel thrashing.

augmented DWA planner are still evident across all scenarios and configurations. Specifically, in challenging cases (e.g., figure-x scenario), baseline-2 achieves optimization with respect to discontinuity crossings, but overall travel time is significantly longer than that of the augmented planner (i.e., aug-DWA-3). The travel-time improvement arises from our optimization that enables the robot to operate away from inefficient regions.

The distance-based scoring mode performs generally better than the simple-scoring mode. The performance difference for exceptions (figure-8 and rectangle scenarios on the physical robot) is statistically insignificant. Performance

difference between forward-only and forward-backward configurations depends on whether the natural travel pattern is amenable to driving in reverse. Specifically, figure-8 and rectangle scenarios seem to prefer the forward-only configuration, whereas the figure-x scenario prefers bidirectional motion. This is expected, because when the next waypoint is behind the robot, the forward only configuration will tend to produce a U-turn with forward-moving velocity, which is a motion pattern likely to trigger the discontinuity crossings.

Fig. 5 shows actual trajectories followed recorded from the physical-robot experiment running in the maze scenario. Traversed paths are well aligned, which means that all configurations are tracking the waypoints produced by the global planner well. Minor variations come from the variations in the global planner output and path tracking performance.

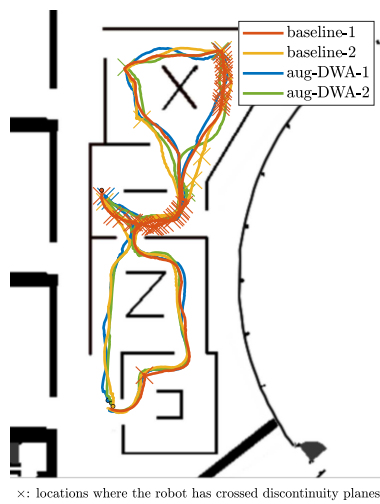


Fig. 5. Actual robot trajectories with two baseline cases and two instances of the augmented DWA planner proposed in this paper. Discontinuity counts: baseline-1: 39 (aborted), baseline-2: 5, aug-DWA-1: 3, aug-DWA-2: 4.

The main performance difference comes from the number of discontinuity crossings depicted by \times -markers in the figure. Baseline configurations are dominated by discontinuity crossings in the upper section of the maze because that is where the robot tends to change the direction of travel or attempts to move sideways. The last segment of the baseline-1 case (red line) is missing because the goal was abandoned. As expected, the number of discontinuity crossings has been dramatically reduced using two instances of the augmented DWA planner.

VI. CONCLUSIONS

Steering constraints of a 4WIS drive introduce discontinuity planes in the 3-dimensional velocity configuration space. Previously reported results have only studied unconstrained steering or side-stepped the constrained-steering problem by using Ackermann steering. To our knowledge, our work is the first that addresses the constrained-steering problem for 4WIS by deriving the discontinuity planes, followed by designing an example planner that uses them as an integral part of decision making.

In our implementation, the local planner scores proposed velocities based on the distance to discontinuity planes and the motion controller stops the motion and flips the wheel if necessary. The planner prefers the velocities that avoid the wheel flip, but it does not eliminate them. The overall behavior depends on other critics in the scoring chains that are used and the relative weights among the critics. We further introduced an additional smoothness critic to cope with the wheel-racing condition that arises if each wheel is controlled with an independent PID controller. Coupled wheel control is the logical follow-up to the presented work and so is a fully dynamic controller. The constraints we derived herein remain valid in both cases.

ACKNOWLEDGMENTS AND NOTES

We thank Liyu Cai, Haiyang Zhang, Yonggang Wang, and Li Yang who built the robot mechanical frame that we used for experiments. Anthony Rodrigues, Andrew Hollabaugh, and Joshua Schmidt implemented hardware and software improvements that enabled the implementation of the presented controller. Larry O’Gorman and Martin Carroll provided invaluable comments that helped us improve the paper.

Extended video demonstration of the results is available at https://youtu.be/819s2Wb_vec.

REFERENCES

- [1] M. F. Selekwa and J. R. Nistler, “Path tracking control of four wheel independently steered ground robotic vehicles,” in *Proc. IEEE Conf. Decision Control*. IEEE, 2011, pp. 6355–6360.
- [2] P. Hang, X. Chen, S. Fang, and F. Luo, “Robust control for four-wheel-independent-steering electric vehicle with steer-by-wire system,” *Int J Automat Technol.*, vol. 18, no. 5, pp. 785–797, 2017.
- [3] P. Hang, Y. Han, X. Chen, and B. Zhang, “Design of an active collision avoidance system for a 4wis-4wid electric vehicle,” *IFAC-PapersOnLine*, vol. 51, no. 31, pp. 771–777, 2018.
- [4] G.-D. Yin, N. Chen, J.-X. Wang, and J.-S. Chen, “Robust control for 4ws vehicles considering a varying tire-road friction coefficient,” *Int J Automat Technol.*, vol. 11, no. 1, pp. 33–40, 2010.
- [5] F.-X. Xu, X.-H. Liu, W. Chen, C. Zhou, and B.-W. Cao, “Improving handling stability performance of four-wheel steering vehicle based on the h2/hinf robust control,” *Applied Sciences*, vol. 9, no. 5, p. 857, 2019.
- [6] M. Lee and T. S. Li, “Kinematics, dynamics and control design of 4wis4wid mobile robots,” *J. Eng.*, vol. 2015, no. 1, pp. 6–16, 2015.
- [7] K. Khairnar, M. Gavani, and S. Nalawade, “Design and control of swerve drive robot using kinematic model,” in *2023 14th International Conference on Computing Communication and Networking Technologies (ICCCNT)*, 2023, pp. 1–5.
- [8] “Zoox company information on the web,” Online Information, available at <https://zoox.com/>.
- [9] “Ottonomy company information on the web,” Online Information, available at <https://ottonomy.io/>.
- [10] “Naio technologies company information on the web,” Online Information, available at <https://www.naio-technologies.com/>.
- [11] “ROS navigation package,” Web Page (ROS documentation), 2020, available at <http://wiki.ros.org/navigation>.
- [12] X. Liu, W. Wang, X. Li, F. Liu, Z. He, Y. Yao, H. Ruan, and T. Zhang, “MPC-based high-speed trajectory tracking for 4WIS robot,” *ISA Transactions*, vol. 123, pp. 413–424, 2022.
- [13] A. Arab, I. Hadžić, and J. Yi, “Safe predictive control of four-wheel mobile robot with independent steering and drive,” in *2021 American Control Conference (ACC)*. IEEE, 2021, pp. 2962–2967.
- [14] D. Fox, W. Burgard, and S. Thrun, “The dynamic window approach to collision avoidance,” *IEEE Robot. Automat. Mag.*, vol. 4, no. 1, pp. 23–33, 1997.
- [15] N. Koenig and A. Howard, “Design and use paradigms for gazebo, an open-source multi-robot simulator,” in *Proc. IEEE/RSJ Int. Conf. Intell. Robot. Syst.*, Sep. 2004, pp. 2149–2154.